Supporting Information

Core-Shell Palladium Nanoparticle@Metal-Organic Frameworks as Multifunctional Catalysts for Cascade Reactions

Meiting Zhao,[†] Ke Deng,[†] Liangcan He,[†] Yong Liu,[†] Guodong Li,*[,†] Huijun Zhao[‡] and Zhiyong Tang*[,†]

[†]Laboratory for Nanomaterials, National Center for Nanoscience and Technology, Beijing, 100190, P. R. China

[‡]Centre for Clean Environment and Energy and Griffith School of Environment, Griffith University, Queensland, 4222, Australia

Experimental Section

1. Reagents

Palladium (II) chloride ($PdCl_2$, 99%) was purchased from Sinopharm. Zinc nitrate hexahydrate ($Zn(NO_3)_2 \cdot 6H_2O$, 99%), 2-amino terephthalic acid (NH_2-H_2BDC, 99%), cetyl trimethyl ammonium chloride (CTAC, 96%), ascorbic acid (AA, > 99%) , sodium borohydride ($NaBH_4$, 98%), polyvinylpyrrolidone (PVP, Mw=8000), 4-nitrobenzaldehyde (99%), 4-nitrocinnamaldehyde (98%), malononitrile (99%) and octodecane (> 99.5%) were provided by Alfa Aesar. N, N-dimethylformamide (DMF) was bought from Sigma-Aldrich. DMF-d7 (99.5%D) and 4-bromo-1-butene (98%) were purchased from J&K. 7-nitroindole-3-carboxaldehyde (95%) was bought from fluorochem. Other analytical grade solvents including dichloromethane (CH_2Cl_2), ethanol and toluene were supplied by Tianjing Chemical Reagent Company (China). All the chemicals were used without further purification.

2. Synthesis of Pd NPs with the diameters of about 35 nm using seeded growth method

Pd NPs were synthesized according to the literature with minor modification.[S1] In a typical procedure, 0.25 mL H_2PdCl_4 (10 mM) was mixed with 9.75 mL CTAC (100 mM). Next, 0.50 mL ice-cooled $NaBH_4$ solution (50 mM) was added into the above solution under vigorous stirring. After that, the resultant solution was kept at room temperature for 3 h and then was used as the seed for further synthesizing larger Pd NPs. Subsequently, 1.80 mL H_2PdCl_4 (10 mM) was added into the mixture solution of 25 mL CTAC (3.6 mM) and 25 mL PVP (Mw = 8000, 1.6 g L^{-1}), followed by adding 0.03 mL seed solution and 0.6 mL ascorbic acid (100 mM). Finally, the reaction solution was stirred gently for 10 seconds and then kept at room temperature overnight. The products were centrifuged at 5000 rpm and 8000 rpm for 10 min, respectively. The obtained Pd NPs were redispersed into 0.5 mL ultrapure water for subsequent growth of IRMOF shells.

3. Synthesis of core-shell Pd@IRMOF-3 nanocomposites

A facile solvothermal method of mixed solvent was introduced to synthesize the core-shell Pd@IRMOF-3 nanocomposites. In a typical procedure, 0.20 g PVP was dissolved into the mixed solvent containing 6 mL DMF and 4 mL ethanol, and then 0.08 mL as-synthesized Pd NPs was added drop by drop into the above solvent under stirring. Next, 22.31 mg $Zn(NO_3)_2$ (0.075 mmol) and 5.43 mg 2-amino terephthalic acid (0.03 mmol) dissolved into 2 mL DMF were added into the above mixed solution. After that, the solution was treated under ultrasonic conditions for 20 min.

Subsequently, the solution was transferred into a 20 mL Teflon-lined stainless steel autoclave and heated at 100 ^{o}C for 240 min. After reaction, the product was collected by centrifugation at 3000 rpm for 10 min. The precipitate was redispersed in 20 mL DMF and heated at 100 ^{o}C for 12 h to remove the unreacted organic ligands and PVP. Finally, the solid material was dispersed in 20 mL CH_2Cl_2 for 12 h, and this procedure was repeated twice for the activation of IRMOF-3.

To elucidate the formation mechanism of the core-shell Pd@IRMOF-3, a series of control experiments were carried out, including variation of PVP amount, ethanol/DMF ratio and crystallization time.

4. Synthesis of IRMOF-3

0.20 g PVP was dissolved into the mixed solvent containing 4 mL DMF and 4 mL ethanol, and then 22.31 mg $Zn(NO_3)_2$ (0.075 mmol) and 5.43 mg NH_2-H_2BDC (0.03 mmol) dissolved in 4 mL DMF were added into the above solution. After that, the solution was treated under ultrasonication for 20 min. Subsequently, the solution was transferred into a Teflon-lined stainless steel autoclave and heated at 100 ^{o}C for 8 h. Finally, the obtained product was collected by centrifugation at 4000 rpm for 15 min. The precipitate was redispersed in 20 mL DMF and heated at 100 ^{o}C for 12 h to remove the unreacted organic ligands and PVP.

5. Synthesis of Pd/IRMOF-3

The synthesized IRMOF-3 was redispersed into 10 mL DMF, and then 0.08 mL as-synthesized Pd NPs was added drop by drop into the above solvent under magnetic stirring. Subsequently, the mixture solution was further stirred at room temperature for 24 h. The obtained IRMOF-3 supported Pd NPs were collected by centrifugation at 4000 rpm for 15 min. Finally, the solid material was dispersed in CH_2Cl_2 for 12 h, and this procedure was repeated twice for the activation of IRMOF-3.

6. Synthesis of 4-nitro-1-butene

4-nitro-1-butene was synthesized according to the literature.[S2] 13 mL anhydrous Et_2O was added into a mixture containing 4.56 g $AgNO_2$ and 1.0 mL 4-bromo-1-butene in a flask protected from light. The reaction mixture was refluxed at 50 ^{o}C for 24 h, and then cooled, filtered, purified by distillation and dried under vacuum. Finally, 4-nitro-1-butene as pale yellow oil was obtained.

^{1}H NMR (400 MHz, $CDCl_3$): δ 5.82-5.71 (m, 1H), 5.20-5.15 (m, 2H), 4.46-4.42 (t, J = 8.0 Hz, 2H), 2.78-2.72 (m, 2H).

7. Evaluation of catalytic performances of different samples for the cascade reactions

The catalytic performance of different samples including Pd@IRMOF-3, Pd/IRMOF-3, pure IRMOF-3 and bare Pd NPs was evaluated by using the cascade reactions of Knoevenagel condensation coupled with subsequent hydrogenation process. In a typical procedure, different catalysts were dispersed into 1 mL DMF, followed by adding 0.2 mmol 4-nitrobenzaldehyde and 0.21 mmol malononitrile. Next, the obtained solution was stirred in a stainless-steel autoclave at room temperature for 20 min to finish the Knoevenagel condensation of 4-nitrobenzaldehyde and malononitrile. Subsequently, the autoclave was purged with H_2 for 4 times, and the H_2 pressure of the autoclave was set at 0.20 MPa for the subsequent hydrogenation process. The reaction solvent was magnetically stirred at room temperature for 24 h. After that, the catalysts were separated by centrifugation, and washed with DMF solution. The obtained organic solvent was diluted with CH_2Cl_2 and then analyzed by GC-MS (Thermo DSQ) using octodecane as an internal standard substance.

8. Characterization

Scanning electron microscopy (SEM) measurement was performed on a Hitachi S4800 scanning electron microscope at 6.0 kV. Transmission electron microscopy (TEM) images were carried out using Tecnai G2 F20 S-TWIN at 200 kV. High angle annular dark field scanning transmission electron microscopy (HAADF-STEM) imaging and energy-dispersive X-ray spectroscopy (EDX) elemental mapping were characterized by FEI Tecnai G2 F20 S-TWIN at 200 kV. Powder X-ray diffraction (XRD) patterns were recorded on D/MAX-TTRIII (CBO) with Cu Kα radiation (λ = 1.542 Å) operating at 50 kV and 300 mA. Brunauer-Emmett-Teller (BET) surface area and pore size of the different samples were measured using a Quadrasorb SI-MP instrument. Fourier transform infrared (FTIR) spectra were recorded on a Spectrum One in the spectral range of 400−4000 cm^{-1} using the KBr disk method.

9. Computational details

Theoretical calculations were performed using density functional theory (DFT) provided by the DMol3 code.[S3] In DMol3, the electronic wave function was expanded in a localized atom-centered basis set with each basis function defined numerically on a dense radial grid. We used the double-numeric polarized (DNP) basis sets.[S4, S5] The Perdew and Wang parameterization of the local exchange-correlation energy were applied in the local spin density approximation (LSDA) to

describe exchange and correlation.[S6] The inner core electrons for Pd were represented by the DFT semilocal pseudo-potential (DSPP) specifically developed for DMol3 calculations, while eighteen electrons were treated explicitly for Pd (those corresponding to the atomic levels 4*s*, 4*p*, 4*d*). Each basis function was restricted to within a cutoff radius of R_{cut} = 5.5 Å. Spin-restricted wave functions were employed. A self-consistent field procedure was done with a convergence criterion of 10-5 a.u. on the energy and electron density.

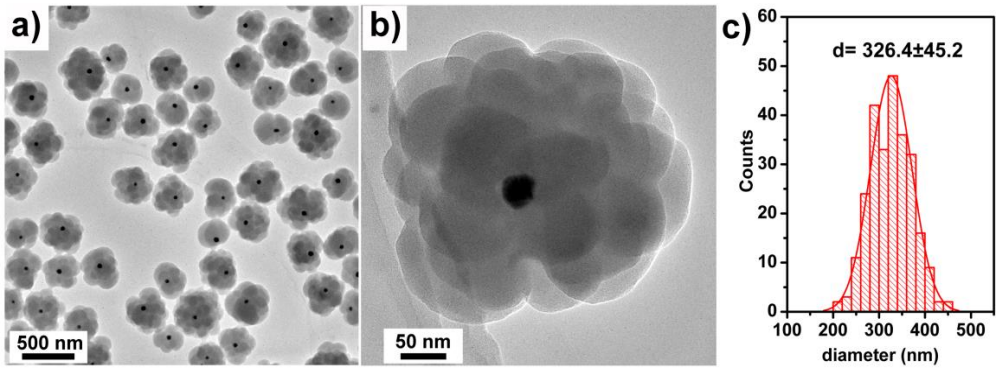

Figure S1. (a) TEM image of core-shell Pd@IRMOF-3 nanocomposites. (b) TEM image of single core-shell Pd@IRMOF-3. (c) The size histogram of the core-shell structures estimated by counting 260 particles in the corresponding TEM images. The Pd NPs in the core-shell structures are about 35 nm in diameter.

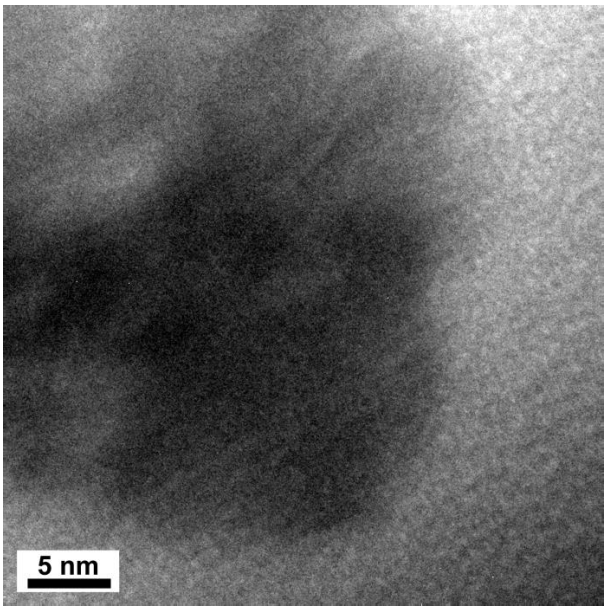

Figure S2. HRTEM image of the core-shell Pd@IRMOF-3 nanocomposites.

It is noted that the atomic images of the Pd core and IRMOF-3 shell are not clearly recognized in HRTEM imaging, likely due to the fact that the Pd NP core is encapsulated by the thick shell and IRMOF-3 is unstable under illumination of high energy electron beam.

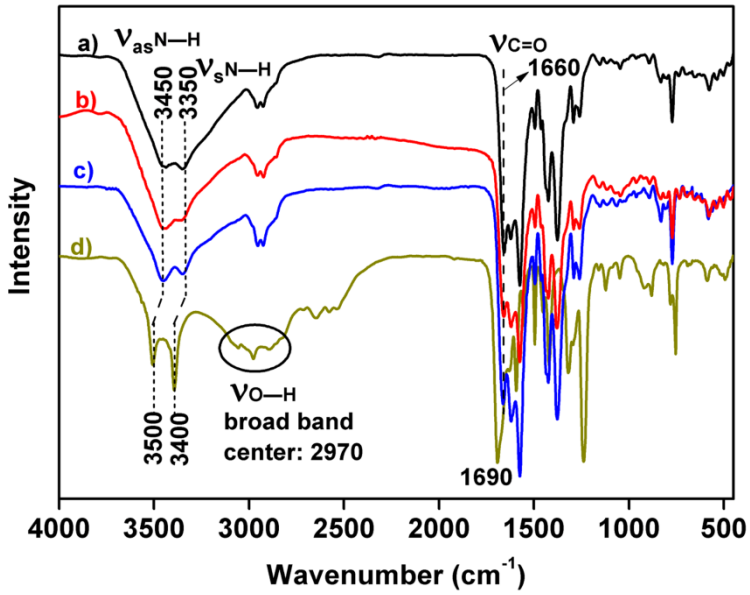

Figure S3. FTIR spectra of (a) Pd@IRMOF-3; (b) Pd/IRMOF-3; (c) IRMOF-3 and (d) organic linker NH_2-H_2BDC.

The stretching vibration peaks of amino group in the Pd@IRMOF-3 (curve a), Pd/IRMOF-3 (curve b) and IRMOF-3 (curve c) samples are down shifted from 3500 cm^{-1} and 3400 cm^{-1} to 3450 cm^{-1} and 3350 cm^{-1} in comparison with the pure NH_2-H_2BDC (curve d), owing to formation of intra-framework hydrogen bonding of amine group with an electron donating oxygen from the carboxylic group.[S7] Furthermore, for all the Pd@IRMOF-3, Pd/IRMOF-3 and IRMOF-3 samples, the characteristic -OH stretching frequency in the carboxylic acid group of the NH_2-H_2BDC linker centered at 2970 cm^{-1} is disappeared, suggesting occurrence of the coordination interaction between Zn^{2+} ions and carboxylic acid group of NH_2-H_2BDC to form IRMOF-3.

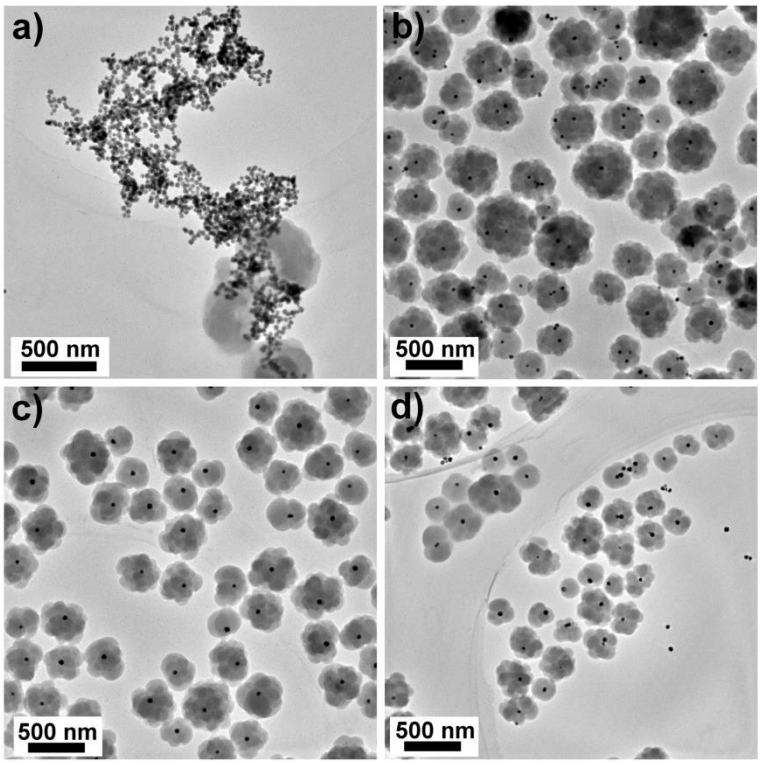

Figure S4. TEM images of the obtained products with different amounts of PVP: (a) 0 g, (b) 0.10 g, (c) 0.20 g, and (d) 0.40 g.

In the absence of PVP in the mixed solvent containing ethanol and DMF, Pd NPs tend to aggregate together and no core-shell nanocomposites are discerned. When 0.1 g PVP is added into the mixed solvent, some of the obtained nanocomposites contain several Pd NP cores, which may be caused by the poor dispersion of Pd NPs using low amount of PVP. At PVP amount of 0.4 g, in addition to the core-shell Pd@IRMOF-3, free Pd NPs are also observed, suggesting the adsorption of the Zn^{2+} and NH_2-H_2BDC onto the PVP-stabilized Pd NPs is partially impeded by the competitive adsorption of excessive PVP molecules.[S8] It is found that the well-defined core-shell Pd@IRMOF-3 nanocomposites could be achieved at PVP amount of around 0.2 g.

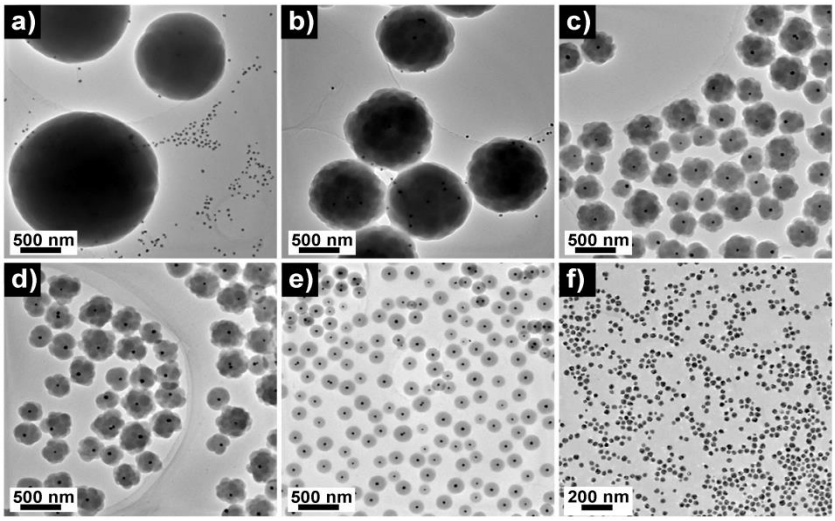

Figure S5. TEM images of the obtained products at various ethanol/DMF volume ratios: (a) 0:1, (b) 0.25:1, (c) 0.5:1, (d) 1:1, (e) 2:1 and (f) 1:0.

At the ratio of ethanol against DMF is no more than 0.25, both free Pd NPs and several Pd cores coated with thick IRMOF-3 shells are observed, likely due to quick growth of IRMOF-3 in the high-ratio DMF in the mixed solvent. On the contrary, when the ratio of ethanol in the mixed solvent is high, the growth speed of IRMOF-3 is obviously slower, for instance, at the ratio of ethanol against DMF is 2, the Pd NP core is only surrounded by a thin shell of amorphous IRMOF-3 (blow Figure S6). This result highlights that one can control the growth of MOF shells on the noble metal NP cores by changing the composition ratio of the mixed solvent.

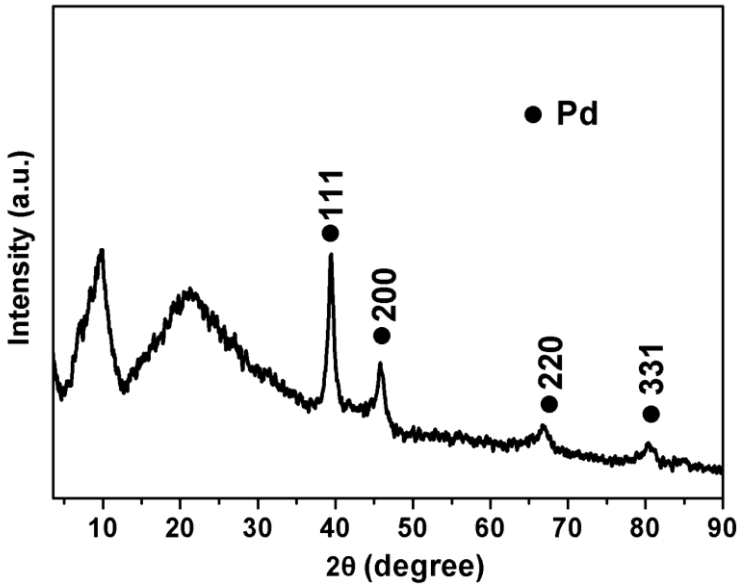

Figure S6. XRD pattern of the core-shell Pd@IRMOF-3 shown in Figure S5e.

The broad diffraction peaks at ~10° and ~20° indicate the amorphous nature of the IRMOF-3 shells obtained at the ethanol/DMF volume ratio of 2.

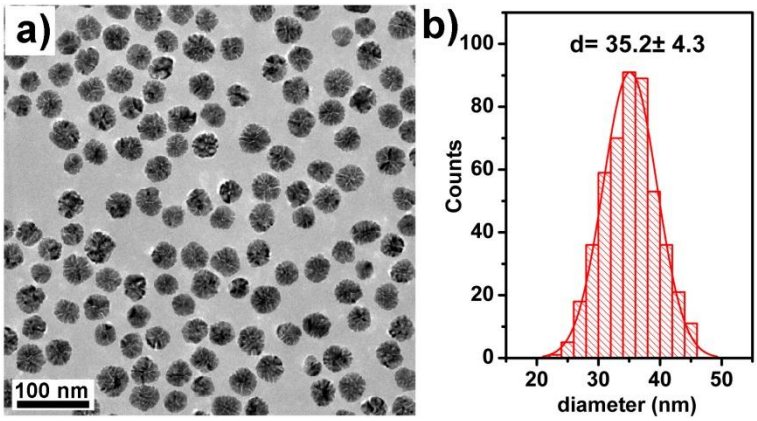

Figure S7. (a) TEM image of the synthesized Pd NPs and (b) corresponding particle size histogram estimated by 490 Pd NPs in the corresponding TEM images.

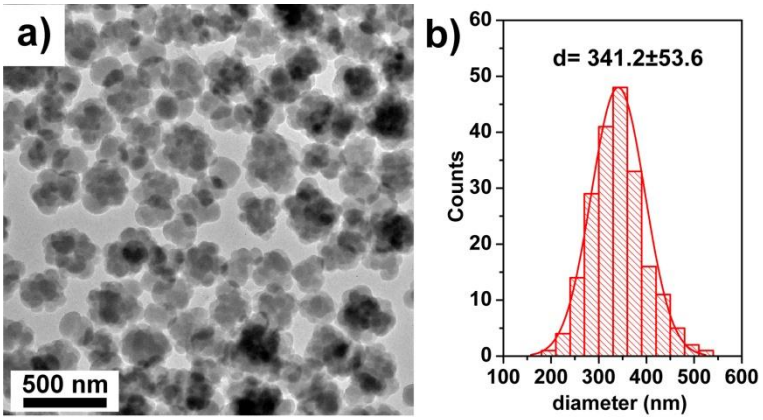

Figure S8. (a) TEM image of the IRMOF-3 NPs. (b) Corresponding particle size histogram estimated by 205 NPs in the TEM images.

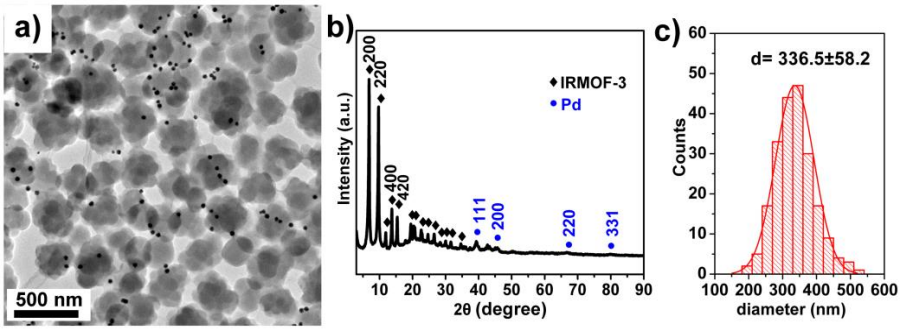

Figure S9. (a) TEM image of the conventional supported Pd/IRMOF-3 nanocomposites. (b) XRD pattern of the Pd/IRMOF-3 nanocomposites. (c) The particle size histogram of Pd/IRMOF-3 estimated by 212 nanocomposites in the corresponding TEM images.

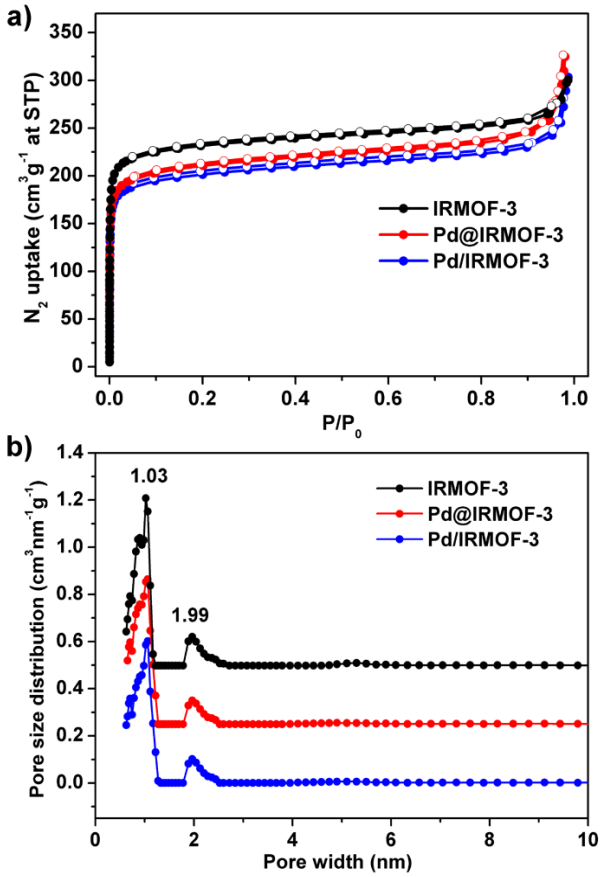

Figure S10. (a) Nitrogen adsorption-desorption isotherm of Pd@IRMOF-3, Pd/IRMOF-3 and pure IRMOF-3 at 77 K up to 1 bar. The solid and open symbols represent adsorption and desorption, respectively. (b) Corresponding pore size distributions calculated by the nonlocal density functional theory (NLDFT) method,[S8] and the original curves for Pd@IRMOF-3 and IRMOF-3 are shifted up by 0.25 and 0.5 for clarity.

N_2 physisorption data indicate that all the samples present the typical type I nitrogen sorption isotherms with the steep increase in N_2 uptake at low relative pressure (< 0.01), and they have the same two micropores that are dominantly composed of those of about 1.03 nm in diameter along with small percentage of about 1.99 nm (below Table S1).

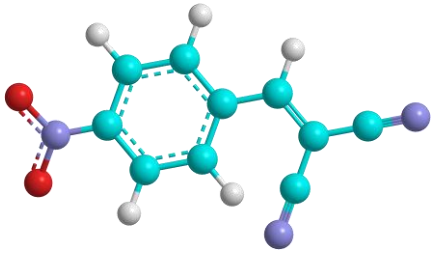

Figure S11. Molecular structure of the intermediate product 2-(4-nitrobenzylidene)malononitrile (**B**) (1.19 nm × 0.79 nm). The blue, purple, red and gray spheres represent C, N, O, and H atoms, respectively.

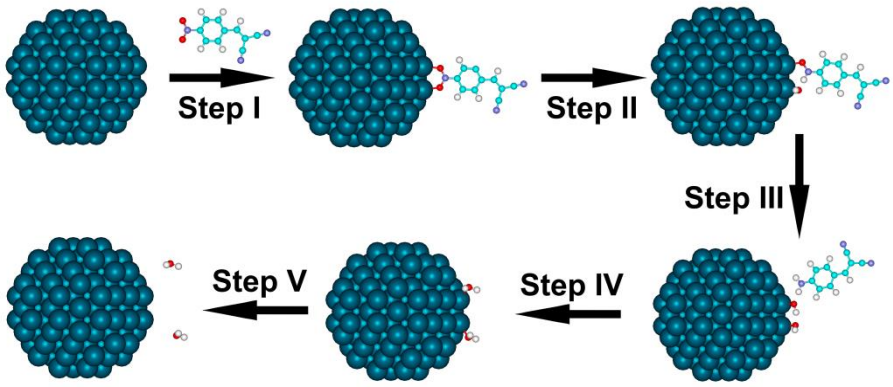

Figure S12. Theoretical models of the hydrogenation conversion from **B** to **C** on bare Pd NPs**.** The large cyan clusters represent the Pd particles, while the blue, purple, red and white small balls stand for C, N, O, and H atoms in 2-(4-nitrobenzylidene)malononitrile (**B**), respectively.

We calculated the Gibbs free energy (ΔG) of the hydrogenation process from **B** to **C** on the bare Pd NPs. We designed a Pd particle with the diameter of 15 Å as the simplified model for the Pd NPs. The hydrogenation reaction of **B** to **C** experiences the adsorption→hydrogenation →desorption process, and corresponding the Gibbs free energy (ΔG) of **B**→**C** is shown as the follows:

(1) $Pd + \mathbf{B} \rightarrow \mathbf{B}_{on\ Pd}$ $\Delta G = -41.91$ kcal mol^{-1}

(2) $\mathbf{B}_{on\ Pd} + H_2 \rightarrow \mathbf{B}\text{-}H_{on\ Pd} + O\text{-}H_{on\ Pd}$ $\Delta G = -39.53$ kcal mol^{-1}

(3) $\mathbf{B}\text{-}H_{on\ Pd} + O\text{-}H_{on\ Pd} + H_2 \rightarrow 2O\text{-}H_{on\ Pd} + \mathbf{C}$ $\Delta G = -41.85$ kcal mol^{-1}

(4) $2O\text{-}H_{on\ Pd} + H_2 \rightarrow 2H_2O_{on\ Pd}$ $\Delta G = -42.14$ kcal mol^{-1}

(5) $2H_2O_{on\ Pd} \rightarrow Pd + 2H_2O$ $\Delta G = 34.66$ kcal mol^{-1}

The total hydrogenation process of **B**→**C** is:

$\mathbf{B} + 3H_2 + Pd \rightarrow \mathbf{C} + 2H_2O + Pd$ $\Delta G = -130.77$ kcal mol^{-1}

The first step is the adsorption process, in which **B** forms a bridged bidentate on the Pd particle surface through the NO_2 group. The second and third steps are the hydrogenation steps occurring on the N-O bonds in sequence, and free **C** is generated. The fourth step is the hydrogenation step occurring on the adjacent O-H adsorbed on Pd surface. The fifth step is desorption of H_2O product from the surface of Pd particles.

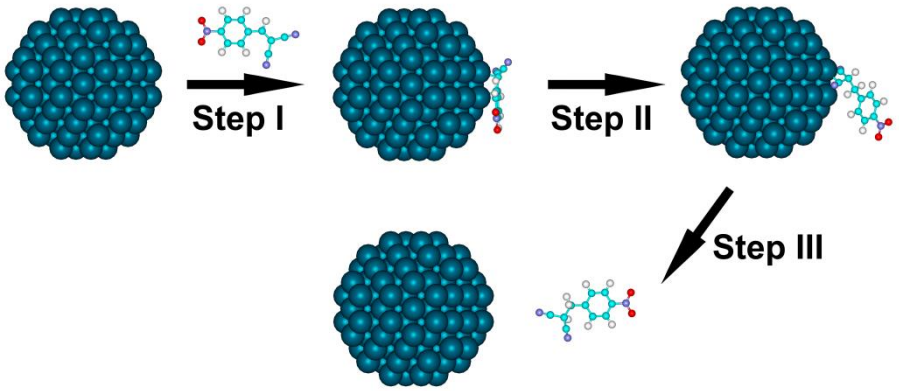

Figure S13. Theoretical models of the hydrogenation conversion from **B** to **D** on bare Pd NPs**.** The large cyan clusters represent the Pd particles, while the blue, purple, red and white small balls stand for C, N, O, and H atoms in 2-(4-nitrobenzylidene)malononitrile (**B**), respectively.

We calculated the Gibbs free energy (ΔG) of the hydrogenation process from **B** to **D** on the bare Pd NPs. We designed a Pd particle with the diameter of 15 Å as the simplified model for the Pd NPs. The hydrogenation reaction of **B** to **D** experiences the adsorption→hydrogenation →desorption process, and the corresponding Gibbs free energy (ΔG) of **B→D** is shown as the follows:

(1) $Pd + \mathbf{B} \rightarrow \mathbf{B}_{on\ Pd}$ $\Delta G = -78.38$ kcal mol^{-1}

(2) $\mathbf{B}_{on\ Pd} + H_2 \rightarrow \mathbf{D}_{on\ Pd}$ $\Delta G = -21.20$ kcal mol^{-1}

(3) $\mathbf{D}_{on\ Pd} \rightarrow Pd + \mathbf{D}$ $\Delta G = 66.17$ kcal mol^{-1}

The total hydrogenation process of **B→D** is:

$\mathbf{B} + H_2 + Pd \rightarrow \mathbf{D} + Pd$ $\Delta G = -33.40$ kcal mol^{-1}

The first step is the adsorption process, in which **B** forms a bridged bidentate on the Pd particle surface through the C=C group. The second step is the hydrogenation step occurring on the C=C bond, and **D** is formed. The third step is the desorption step, and the adsorbed **D** becomes free.

DFT calculations show that the Gibbs free energy (ΔG) of **B** to **C** is -130.77 kcal mol^{-1}, which is much lower than that of -33.40 kcal mol^{-1} for hydrogenation of **B** to **D** over bare Pd NPs (Figures S11-S13). This indicates that thermodynamically, **C** is the better selective product in the hydrogenation process, which is in good agreement with our experimental observation.

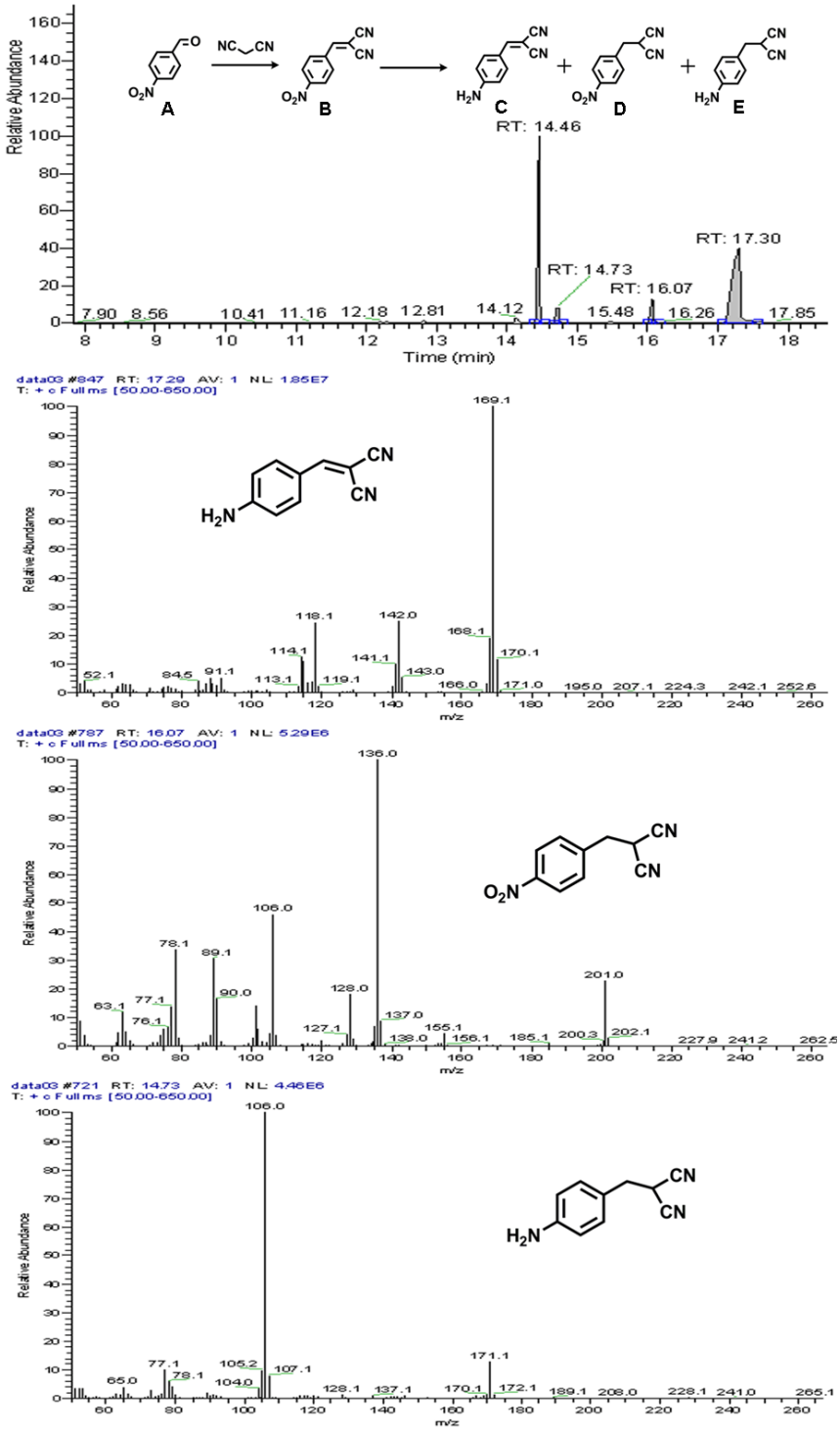

Figure S14. GC-MS results of Knoevenagel condensation of 4-nitrobenzaldehyde (**A**) and malononitrile, and subsequent hydrogenation reaction catalyzed by the core-shell Pd@IRMOF-3 nanocatalysts. It is seen that the core-shell Pd@IRMOF-3 nanostructures can catalyze the cascade reactions completely. As for the hydrogenation process, the selectivity of **B** to **C**, **D** and **E** is 86%, 8%, and 6%, respectively. It should be pointed out that the sharp peak around 14.46 min in the GC spectrum corresponds to the internal standard substance octodecane.

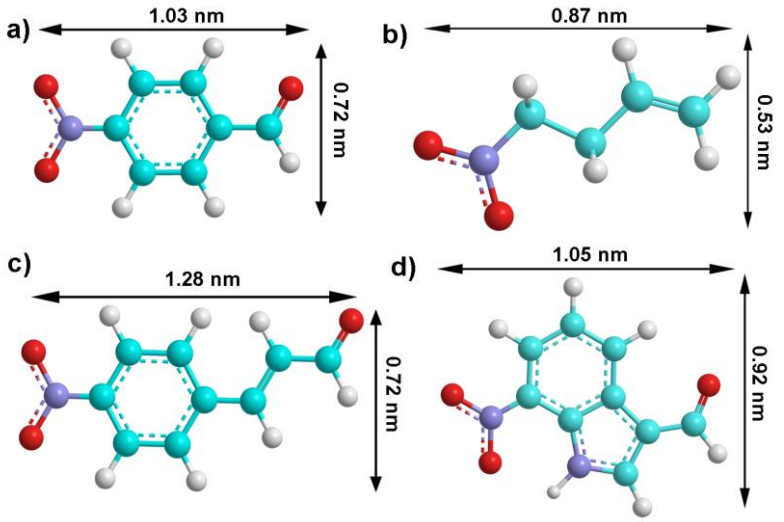

Figure S15. Molecular structure of (a) 4-nitrobenzaldehyde (1.03 nm × 0.72 nm), (b) 4-nitro-1-butene (0.87 nm × 0.53 nm), (c) 4-nitrocinnamaldehyde (1.28 nm × 0.72 nm), and (d) 7-nitroindole-3-carboxaldehyde (1.05 nm × 0.92 nm). The blue, purple, red and gray spheres represent C, N, O, and H atoms, respectively.

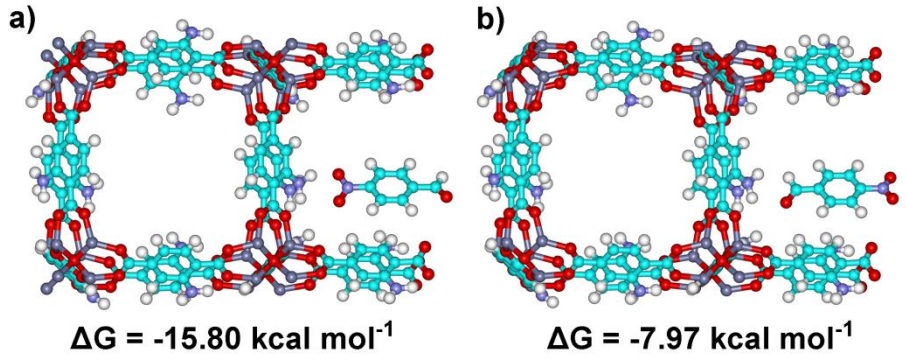

Figure S16. Theoretical models of the interaction between the different end groups of **A** and the NH_2 groups of the IRMOF-3. (a) Compound **A** enters with the NO_2 group ahead, and (b) Compound **A** enters with the C=O group ahead. The gray, blue, purple, red and white small balls stand for Zn, C, N, O, and H atoms, respectively.

DTF calculations indicate that the -NH_2 groups on the surface of IRMOF-3 show an energetically preferable interaction with the -NO_2 groups of **A**, 7.83 kcal mol^{-1} lower than that of the C=O groups of **A**. Accordingly, when the core-shell Pd@IRMOF-3 hybrids are used as the catalysts, **A** prefers entering into the nanostructures with the -NO_2 group ahead.

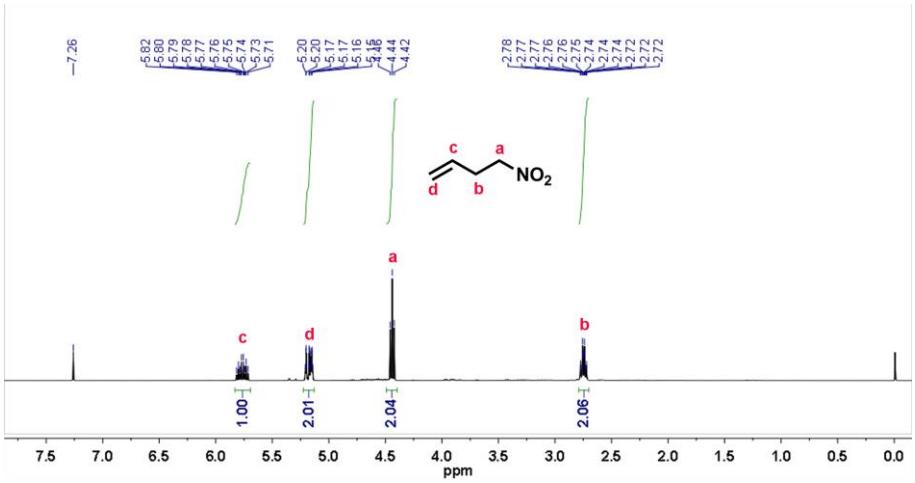

Figure S17. ^{1}H NMR spectrum of as-synethesized 4-nitro-1-butene.

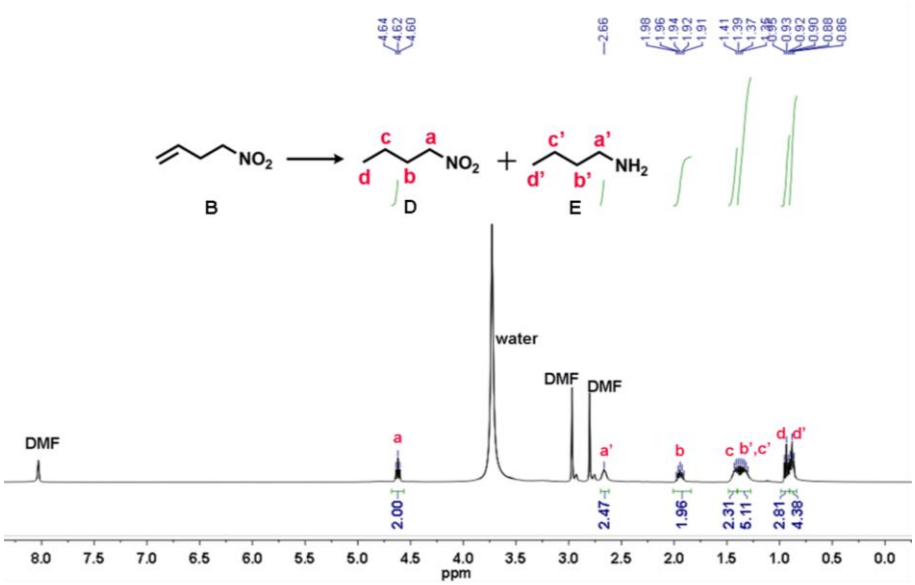

Figure S18. ^{1}H NMR spectrum of the hydrogenation reaction products of 4-nitro-1-butene.

When 4-nitro-1-butene is used as substrate for hydrogenation reaction, both products of 4-amino-1-butane and 4-nitro-1-butane are observable, and the corresponding selectivities are 56% and 44%, respectively. It should be pointed out that the former value is estimated by the ratio of the peak area of a' to that of a plus a', while the latter value is estimated by the ratio of the peak area of a to that of a plus a'.

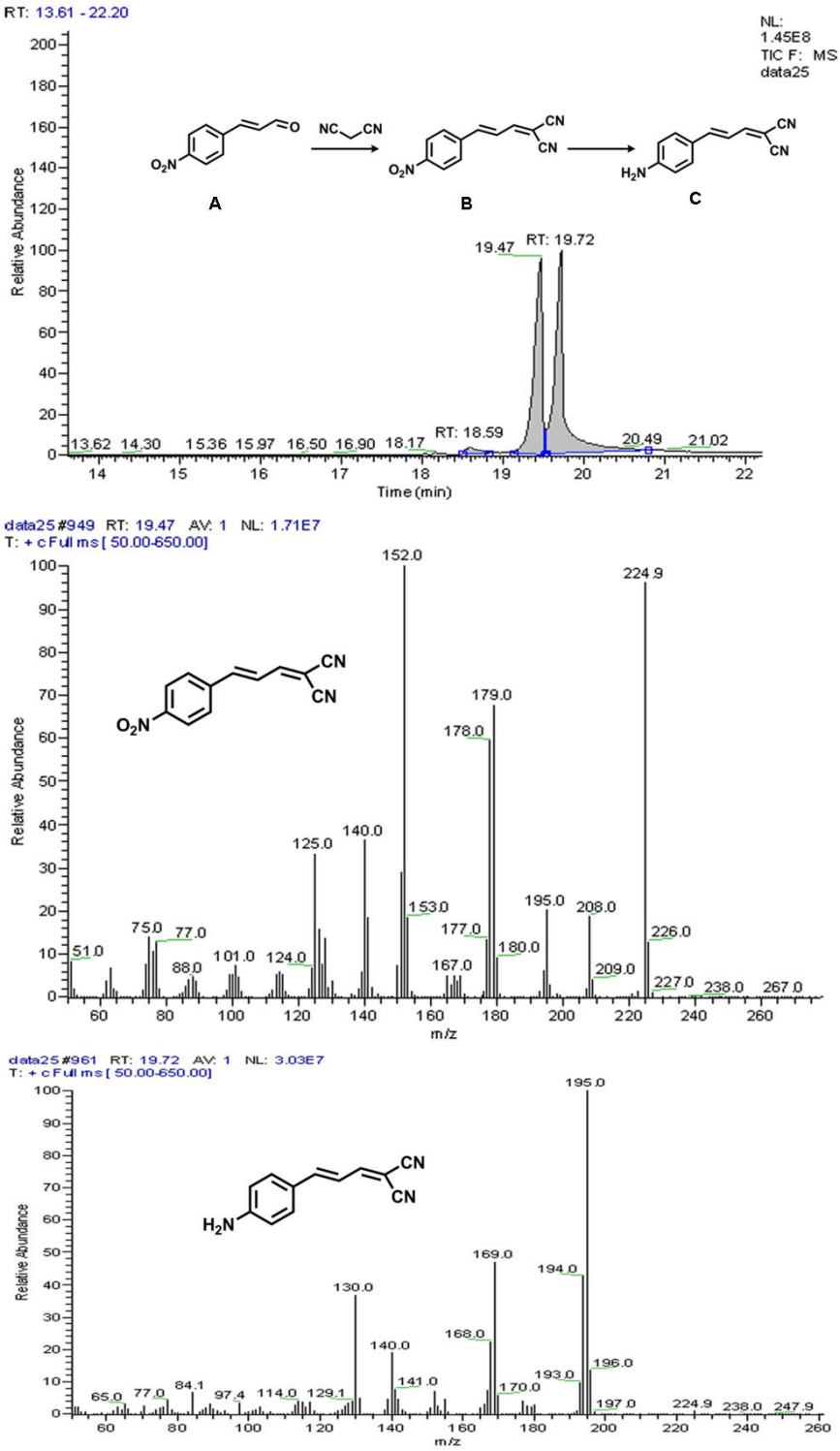

Figure S19. GC-MS results of Knoevenagel condensation of 4-nitrocinnamaldehyde and malononitrile, and subsequent hydrogenation reaction catalyzed by core-shell Pd@IRMOF-3 nanocatalysts. It is seen that the Knoevenagel condensation is carried out completely, and the subsequent hydrogenation reaction is mainly occurred on conversion of -NO_2 into -NH_2 with the corresponding conversion of **B** and selectivity of **C** are 52% and 96%, respectively.

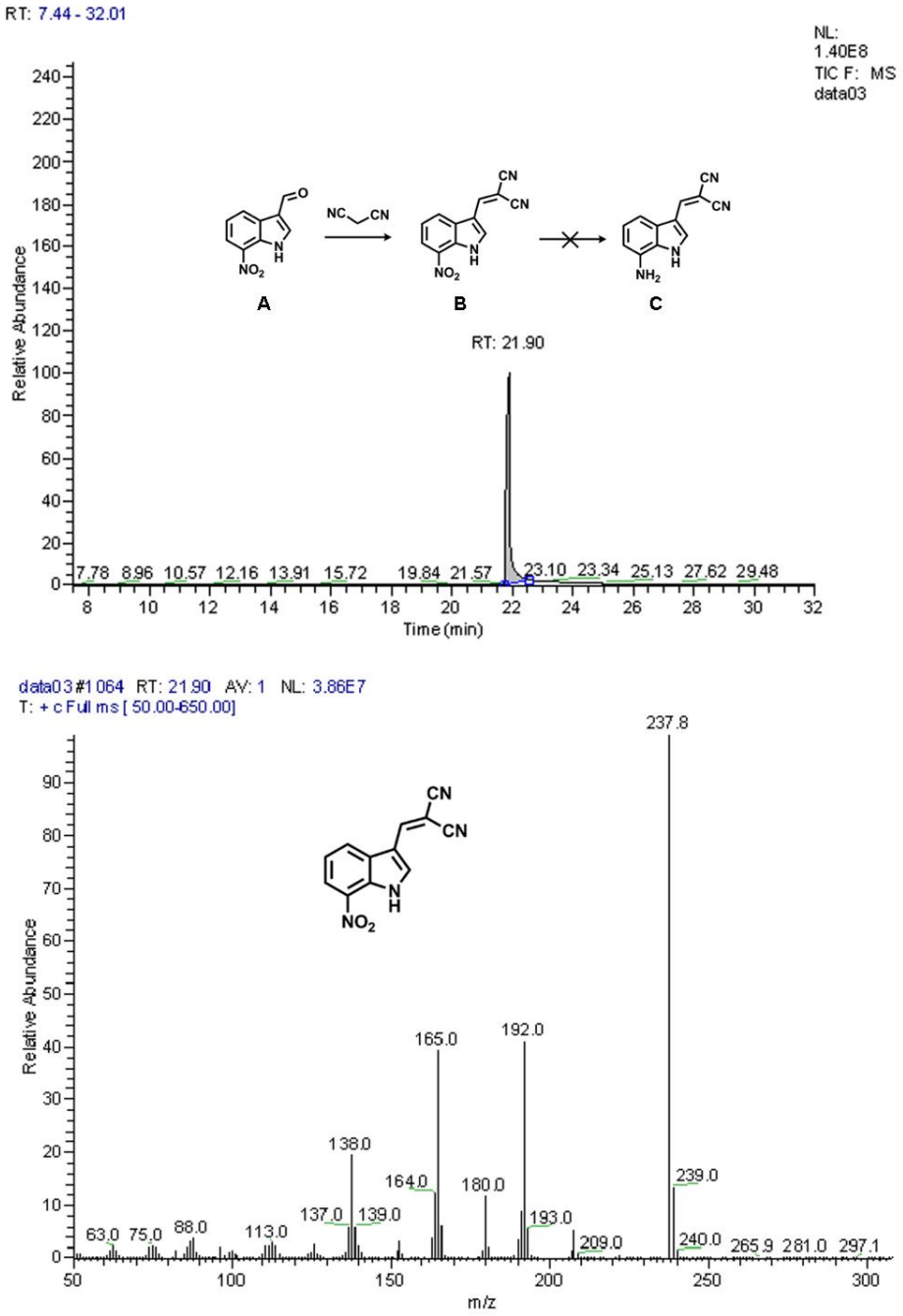

Figure S20. GC-MS results of Knoevenagel condensation of 7-nitroindole-3-carboxaldehyde and malononitrile, and subsequent hydrogenation reaction catalyzed by core-shell Pd@IRMOF-3 nanocatalysts. It is seen that the Knoevenagel condensation is carried out completely, while the hydrogenation reaction does not occur.

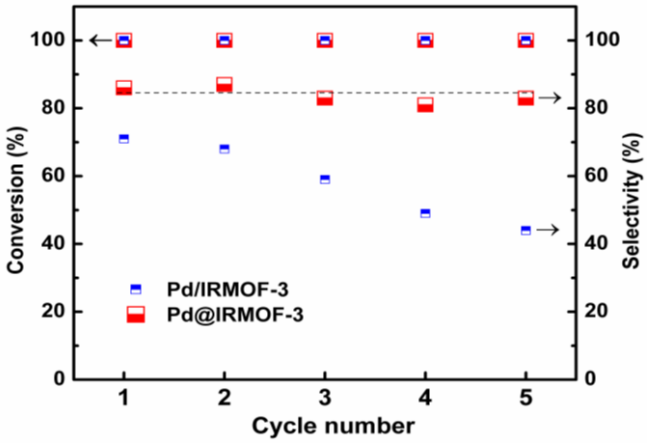

Figure S21. Stability of Pd@IRMOF-3 and Pd/IRMOF-3 nano-composites for catalytic the cascade reactions of Knoevenagel condensation of 4-nitrobenzaldehyde (**A**) and malononitrile coupling with subsequent selective hydrogenation of the intermediate product **B** to the target product **C** over five successive cycles.

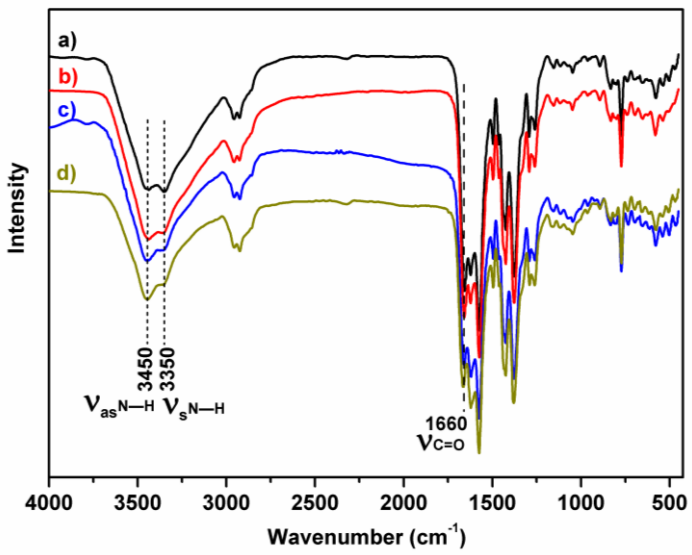

Figure S22. FTIR spectra of fresh and used samples after five successive cycles. a) fresh and b) used Pd@IRMOF-3; c) fresh and d) used Pd/IRMOF-3.

There are no obvious changes in FTIR spectra of IRMOF-3 in both Pd@IRMOF-3 and Pd/IRMOF-3 samples after five successive catalysis cycles, demonstrating the high stability of IRMOF-3.

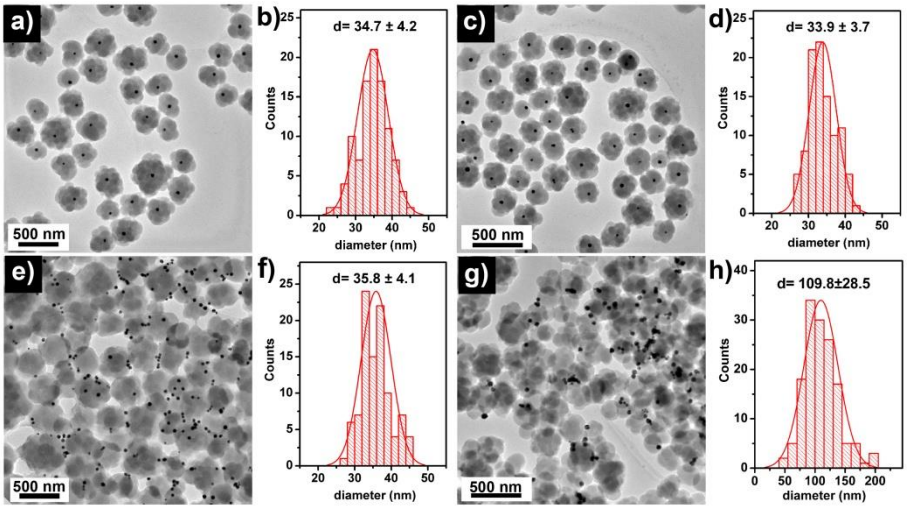

Figure S23. TEM images of different catalysts before (a, e) and after five successive cycles (c, g) for the cascade reactions. (b, d, f and h) Corresponding particle size histogram of Pd NPs. (a-d) for Pd@IRMOF-3; (e-h) for Pd/IRMOF-3.

TEM observations show that there are no obvious changes in the size, shape and structure of the core-shell Pd@IRMOF-3 nanostructures over five successive cycles (Figure S23a-d). On the contrary, the migration and sintering of Pd NPs of about 35 nm in diameter into larger sizes of about 109 nm for the supported Pd/IRMOF-3 samples occurred during the repeated reactions (Figure S23e-h).

Table S1. Physiochemical properties of core-shell Pd@IRMOF-3, supported Pd/IRMOF-3, and pure IRMOF-3.

Catalysts	Pd		IRMOF-3 (nm)	BET surface area[b] ($m^2 g^{-1}$)	Average pore diameter [b] (nm)	Pore volume distributionc ($cm^3 g^{-1}$)	
	Content[a] (wt%)	Diameter (nm)				0.62-1.32 nm	1.79-2.52 nm
Pd@IRMOF-3	2.5	35	325	828	1.03, 1.99	0.265	0.038
Pd/IRMOF-3	2.3	35	336	795	1.03, 1.99	0.255	0.037
IRMOF-3	–	–	341	918	1.03, 1.99	0.292	0.041

[a] Pd content was determined by the inductively coupled plasma mass spectrometry (ICP-MS); [b] Surface areas and pore size distributions of the samples were calculated by using the Brunauer-Emmett-Teller (BET) equation and the nonlocal density functional theory (NLDFT) model,[S9] respectively. [c] The corresponding pore volume distribution is given in the table according to the pore size distribution in Figure S10.

Table S2. Cascade reactions of Knoevenagel condensation coupling with selective hydrogenation reactions of different substrates catalyzed by core-shell Pd@IRMOF-3.[a]

Substrates	$\mathbf{A}_{Conv.}$ (%)	**B**		Sel. (%)		
		Formed[b] (%)	Conv.[c] (%)	**C**	**D**	**E**
4-nitro-1-butene[d]	–	–	100	0	44	56
4-nitrocinnamaldehyde	100	100	52	96	4 (the others)	
7-nitroindole-3-carboxaldehyde	100	100	0	0	0	0

[a]Reaction conditions: **A** (0.2 mmol), malononitrile (0.21 mmol), catalyst (10 mg). [b]**B** is formed via the Knoevenagel condensation reaction. [c]The formed **B** is converted via the hydrogenation reaction. [d]Reaction is taken placed in DMF-d7, and the conversion and selectivity is estimated based on ^{1}H NMR spectra.

References

(S1) Wang, F.; Li, C.; Sun, L.-D.; Xu, C.-H.; Wang, J.; Yu, J. C.; Yan, C.-H. *Angew. Chem. Int. Ed.* **2012**, *51*, 4872.

(S2) Addo, J. K.; Teesdale-Spittle, P.; Hoberg, J. O. *Synthesis*, **2005**, *2005*, 1923.

(S3) Becke, A. *J. Chem. Phys.* **1988**, *88*, 2547.

(S4) Delley, B. *J. Chem. Phys.* **2000**, *113*, 7756.

(S5) Delley, B. *J. Chem. Phys.* **1990**, *92*, 508.

(S6) Perdew, J.; Wang, P. Y. *Phys. Rev. B* **1992**, *45*, 13244.

(S7) Gascon, J.; Aktay, U.; Hernandez-Alonso, M. D.; van Klink, G. P. M.; Kapteijn, F. *J. Catal.* **2009**, *261*, 75.

(S8) Lu, G.; Li, S.; Guo, Z.; Farha, O. K.; Hauser, B. G.; Qi, X.; Wang, Y.; Wang, X.; Han, S.; Liu, X.; DuChene, J. S.; Zhang, H.; Zhang, Q.; Chen, X.; Ma, J.; Loo, S. C. J.; Wei, W. D.; Yang, Y.; Hupp, J. T.; Huo, F. *Nat. Chem.* **2012**, *4*, 310.

(S9) Moellmer J.; Celer, E. B.; Luebke, R.; Cairns, A. J; Staudt, R.; Eddaoudi, M.; Thommes, M. *Micropor. Mesopor. Mater.* **2010**, *129*, 345.